

Short-Term Turbulence Prediction for Seeing Using Machine Learning

MARY JOE MEDLEJ,¹ RAHUL SRINIVASAN,^{2,3} SIMON PRUNET,¹ AZIZ ZIAD,¹ AND CHRISTOPHE GIORDANO¹

¹*Université Côte d'Azur, Observatoire de la Côte d'Azur, J.L. Lagrange, Parc Valrose 06108 Nice Cedex 2, France*

²*SISSA, Via Bonomea 265, 34136 Trieste, Italy*

³*IFPU - Institute for Fundamental Physics of the Universe, Via Beirut 2, 34014 Trieste, Italy*

ABSTRACT

Optical turbulence, driven by fluctuations of the atmospheric refractive index, poses a significant challenge to ground-based optical systems, as it distorts the propagation of light. This degradation affects both astronomical observations and free-space optical communications. While adaptive optics systems correct turbulence effects in real-time, their reactive nature limits their effectiveness under rapidly changing conditions, underscoring the need for predictive solutions. In this study, we address the problem of short-term turbulence forecasting by leveraging machine learning models to predict the atmospheric seeing parameter up to two hours in advance. We compare statistical and deep learning approaches, with a particular focus on probabilistic models that not only produce accurate forecasts but also quantify predictive uncertainty, crucial for robust decision-making in dynamic environments. Our evaluation includes Gaussian processes (GP) for statistical modeling, recurrent neural networks (RNNs) and long short-term memory networks (LSTMs) as deterministic baselines, and our novel implementation of a normalizing flow for time series (FLOTS) as a flexible probabilistic deep learning method. All models are trained exclusively on historical seeing data, allowing for a fair performance comparison. We show that FLOTS achieves the best overall balance between predictive accuracy and well-calibrated uncertainty.

1. INTRODUCTION

Optical turbulence (OT) refers to the random fluctuations in the refractive index of the atmosphere caused by variations in temperature, pressure, and wind. These fluctuations distort the propagation of light through the atmosphere, posing a fundamental limitation to the performance of ground-based optical systems. OT affects many applications, from astronomy to free-space optical (FSO) communication, by degrading image quality or disrupting signal transmission.

In astronomical observations, particularly with extremely large telescopes (ELTs), turbulence introduces distortions in starlight as it passes through the Earth's atmosphere, significantly reducing image quality, which is commonly quantified by the seeing parameter ϵ (Roddier 1981; Tokovinin 2002). The seeing parameter is defined as the full width at half-maximum of the long-exposure, seeing-limited point spread function (PSF) of a star image formed at the focus of a large-aperture telescope, primarily caused by atmospheric turbulence.

Similarly, in FSO communication, turbulence causes signal scattering and intensity fluctuations, thereby reducing the reliability and efficiency of high-speed optical data transmission.

To compensate for the real-time effects of turbulence, adaptive optics (AO) systems have been widely deployed in both fields. AO dynamically corrects wavefront errors using deformable mirrors controlled by feedback from wavefront sensors (Roddier 1999). While AO has significantly improved system performance, it remains inherently reactive and limited by the unpredictability of turbulence over short timescales (Tyson 2002; Khalighi & Uysal 2014a; Wang et al. 2018). This limitation has motivated growing interest in OT forecasting, which can enhance AO performance by enabling predictive corrections or proactive operational adjustments.

In astronomy, turbulence prediction is crucial for optimizing observation scheduling and improving AO performance, thereby maximizing the scientific output of telescopes. Long-term predictions support observatory planning, including telescope scheduling and resource allocation, by providing insight into upcoming observing conditions. Accurate short-term predictions, on the other hand, enable real-time adjustments to AO sys-

tems and observation strategies, ensuring optimal image quality under changing atmospheric conditions. In FSO communication, turbulence prediction is equally important. Long-term predictions assist with network planning and resource optimization, ensuring reliable connectivity over extended periods. Short-term forecasts allow real-time adaptation of system parameters, such as power control and beam tracking, to maintain stable communication links (Khalighi & Uysal 2014b; Majumdar 2015). Together, long-term and short-term predictions play complementary roles in addressing the challenges posed by atmospheric turbulence.

Traditional numerical simulations based on physical models of atmospheric dynamics have produced promising results for long-term turbulence prediction (Frehlich et al. 2010; Giordano et al. 2013; Cherubini & Businger 2013; Giordano et al. 2014; Masciadri et al. 2017; Rafalimanana et al. 2019; Lyman et al. 2020; Rafalimanana et al. 2021; Cherubini et al. 2021a; Giordano et al. 2021; Rafalimanana et al. 2022). However, their high computational cost makes them unsuitable for rapid short-term forecasting, highlighting the need for faster predictive approaches.

Machine Learning (ML) methods offer strong predictive capabilities combined with fast inference, making them particularly well-suited for modeling the complex and rapidly evolving nature of atmospheric turbulence. In this work, we focus on short-term turbulence prediction and investigate ML models for forecasting the seeing parameter with prediction horizons of up to two hours. By leveraging modern data-driven approaches, we aim to improve the accuracy and efficiency of short-term turbulence forecasting for both astronomical observations and FSO communication systems.

Previous studies have demonstrated the potential of ML approaches for atmospheric seeing prediction. Ni et al. (2022) investigated several data-driven techniques for this task. Cherubini et al. (2021b) applied ML methods to forecast seeing conditions for the following five nights. Giordano et al. (2020) used the Random Forest (RF) algorithm to predict seeing with a lead time of up to two hours, while Masciadri et al. (2019, 2023) combined autoregressive models and RF for seeing prediction. Similarly, Milli et al. (2019) explored multilayer perceptrons and RF for short-term forecasts within a two-hour window. Kornilov (2015) treated seeing prediction as an autoregressive problem and applied a linear autoregressive integrated moving average (ARIMA) model.

Building upon these works, our study compares two main categories of models for short-term seeing prediction: statistical models and deep learning models. A

key aspect of this work is the inclusion of probabilistic models within both categories. Unlike deterministic approaches that provide only a single forecast value, probabilistic models also estimate the uncertainty associated with predictions, which is particularly important in atmospheric sciences due to the intrinsic variability of the atmosphere. To evaluate the benefits of probabilistic forecasting, deterministic models are also included for comparison.

Within the statistical category, we employ Gaussian Processes (GP), a probabilistic model that naturally provides both predictions and confidence intervals (Section 3.3). In the deep learning category, we consider both deterministic and probabilistic architectures. Recurrent neural networks (RNNs) and long short-term memory networks (LSTMs) serve as deterministic baselines designed to capture temporal dependencies in sequential data (Sections 3.1 and 3.2). For probabilistic deep learning, we use a normalizing-flow-based model for time series, hereafter referred to as FLOTS, which is capable of modeling complex non-Gaussian distributions (Section 3.4).

A normalizing flow is a class of generative neural networks that models a probability distribution by transforming a simple base distribution (typically a standard Gaussian) into a more complex target distribution through a sequence of invertible and differentiable mappings. This invertible transformation also enables sampling from the learned distribution by drawing samples from the latent space and mapping them back to the data space.

By incorporating GP and FLOTS, our framework integrates probabilistic modeling into both statistical and deep learning approaches. These models provide not only accurate point predictions but also meaningful estimates of predictive uncertainty, which are essential for reliable decision-making in atmospheric applications.

To ensure a fair comparison, all models are trained using only historical seeing measurements without incorporating additional atmospheric or instrumental variables. This minimalist setup isolates the predictive capability of each model under identical data conditions. Including additional features such as temperature, wind, or humidity would increase both complexity and stochasticity, making information integration more challenging (Ni et al. 2022). We leave the exploration of such multivariate models to future work.

The remainder of this paper is organized as follows. Section 2 introduces the dataset and preprocessing steps used for model training. Section 3 describes the forecasting models and their architectures, including the selection of optimal input lengths (Section 3.5) and the

calibration procedure (Section 3.6). Section 4 presents the statistical evaluation of the models, while Section 4 provides case studies illustrating model behavior in specific forecasting scenarios. Finally, Section 5 summarizes the main findings of this study.

2. DATA ACQUISITION AND PREPARATION

2.1. Data Acquisition

The Maunakea Weather Center (MKWC) provided the data used in this study. Observations were collected using a Monitoring Device (MD), which combines the Multi-Aperture Scintillation Sensor (MASS) and the Differential Image Motion Monitor (DIMM) (Vernin & Munoz-Tunon 1995; Kornilov et al. 2007). The MD is located at the summit of Maunakea, a site globally recognized for its exceptional astronomical observing conditions, including dark skies due to minimal light pollution, excellent seeing, low humidity, high elevation (4,205 meters), and a position above most atmospheric water vapor. These characteristics make Maunakea one of the most important astronomical sites in the world. The MD is installed at the top of the Canada-France-Hawaii Telescope (CFHT) instrument tower, approximately 7 meters above the ground (Lyman et al. 2020). It is strategically positioned between the Gemini and CFHT observatories. It is minimally affected by terrain or nearby structures when winds originate from the west or east (Silva 2012). The data have been available since mid-2009 and are continuously updated. Real-time MD data are publicly available through the Maunakea Weather Center website¹. In this study, we used DIMM seeing data between September 2009 and November 2024. DIMM measures the integrated optical turbulence across the entire atmosphere, estimating the total atmospheric seeing. The seeing data range on the Maunakea summit varies between 0.04'' and 5''.

2.2. Data Preparation

Most standard ML models, including RNNs and LSTMs, assume that the input sequence is sampled at regular time intervals (Lipton et al. 2015; Che et al. 2018). This assumption is inherent to the recursive formulation of these models, where each time step corresponds to a uniform update in time (Goodfellow et al. 2016). In our case, we chose a sampling rate of 10 minutes, which aligns with the practical needs of astronomical operations and FSO communication systems (Turchi et al. 2022; Masciadri et al. 2023). High-frequency variability on shorter timescales is generally less relevant for

seeing prediction, since such rapid fluctuations fall outside the response timescales of observatory operations and the real-time adaptability of FSO systems. Astronomers prioritize understanding trends, whether the seeing is increasing, decreasing, or remaining stable, so they can make informed decisions about adjusting observation modalities or scientific programs. In FSO communication, this interval similarly captures turbulence trends critical for maintaining signal quality, enabling effective real-time adjustments.

To prepare the atmospheric seeing data for machine learning modeling, we performed temporal interpolation and resampling to regularize the time series before splitting it into training, validation, and testing sets. The raw seeing measurements were recorded at approximately 1-minute intervals but occasionally contained gaps, which pose challenges for models that expect fixed time steps. To address this, we interpolated the data onto a uniform time grid with a fixed 10-minute sampling interval. The resampling and interpolation procedure consisted of the following steps:

- i Segmentation of continuous time blocks: We calculate the time difference between consecutive pairs of measurements. A new segment is initiated when the gap between measurements exceeds 10 minutes. Hence, every segment contains a continuous block of data without large gaps.
- ii Definition of target grid: Within each segment, we create a time grid with a 10-minute interval. These time steps are the targets for interpolation.
- iii Local bin interpolation with linear regression: Around each target time step, we defined a bin centered at that point, extending one sampling interval on either side. Data points within each bin are used to estimate the interpolated value at the center. We performed linear regression on the bin's time indices (converted to seconds relative to the bin start) and their corresponding seeing values. The regression model was then evaluated at the target time to obtain the interpolated value.
- iv Assembly of the interpolated dataset: All interpolated values were compiled into a new time series with uniform 10-minute spacing. This regularized dataset ensures compatibility with machine learning models that require fixed-size input windows and consistent temporal structure.

For the LSTM, RNN, and FLOTS models, each continuous segment of data was processed independently. Given sufficiently large continuous lengths, the data are

¹ <http://mkwc.ifa.hawaii.edu/current/seeing/>

segmented into input-output pairs, denoted by $\epsilon_- \in \mathbb{R}^{d_-}$ and $\epsilon_+ \in \mathbb{R}^{d_+}$, corresponding to sequence lengths d_- and d_+ , respectively. The input ϵ_- represents a sequence of historical seeing measurements used for prediction, while ϵ_+ is the corresponding future window that the model aims to forecast. The slicing was performed using a sliding window mechanism with a single timestep stride, ensuring that all valid subsequences within a group were extracted. We evaluated different input sequence lengths, testing durations from 6 hours (corresponding to 36 time steps) down to 2 hours (12 time steps), as described in Section 3.5. The output horizon ϵ_+ was fixed at 2 hours (12 time steps), aligned with the predictive goal of the study.

After generating the complete set of (ϵ_-, ϵ_+) pairs, a total of 71 906 pairs were obtained. Each pair corresponds to a two-hour sequence composed of 12 time steps with a temporal resolution of 10 minutes. The dataset therefore represents approximately 143 812 hours of time series data (about 5 992 days).

The resulting pairs were randomly shuffled and split into 81.5% for training (58 603 pairs), 8.5% for validation (6 112 pairs), and 10% for testing (7 191 pairs). This randomization was applied across all valid sequences, ensuring statistical consistency and reducing potential bias in performance evaluation. For the GP model, which operates on fixed input-output pairs without requiring sequence history or internal state memory, the same data preprocessing steps were followed to ensure comparability. Each (ϵ_-, ϵ_+) pair was constructed according to the same input and output lengths used for the deep learning models. However, unlike the deep learning models, the GP implementation does not require a fixed training/validation/test split to operate. Instead, random batches were sampled from the ϵ_- dataset to estimate the GP hyperparameters. These hyperparameters were then kept fixed and used to generate predictions for each batch individually, producing the corresponding ϵ_+ forecasts (Section 3.3). In principle, separating the data used for hyperparameter learning from the data used for prediction also helps prevent overfitting in GP models, as in other machine learning approaches.

This approach preserves the temporal structure of the original data while enforcing consistent time steps. The local linear regression within sliding bins provides a simple and robust way to handle nonuniform sampling while avoiding interpolation across large observational gaps. It is also noteworthy that no normalization was applied to the input data. Since the only feature used in the model is the seeing value, which naturally ranges between approximately 0.04" and 5" (Section 2.1), the scale of the input is already constrained and physically

meaningful. Normalization is typically applied when features have different units, scales, or orders of magnitude to ensure numerical stability during model training. In this case, the seeing values are homogeneous, bounded, and consistent across samples, allowing the models to learn effectively without additional rescaling.

3. METHODS

The goal of this study is to predict atmospheric seeing using forecasting techniques. Atmospheric seeing is affected by turbulent fluctuations in the atmosphere, which are both random and time-dependent. Accurately forecasting seeing therefore requires models that can process sequential data, capture complex temporal dynamics, and, ideally, provide uncertainty estimates to quantify prediction confidence.

We first investigated recurrent neural network architectures, namely RNNs and LSTMs (Sherstinsky 2020), which are widely used for sequential forecasting tasks. RNNs process input data step by step, using prior outputs to inform future predictions (Jain & Medsker 1999). LSTMs extend this capability by retaining information over longer time horizons (Hochreiter & Schmidhuber 1997a; Yu et al. 2019), making them particularly effective for modeling temporal dependencies in atmospheric turbulence. These models showed good predictive performance when trained on past seeing measurements. However, both approaches are deterministic and produce only point predictions, without providing a measure of uncertainty. This limitation can be problematic in operational contexts such as telescope scheduling or optical communication, where reliable confidence intervals are important.

To address this limitation, we also considered Gaussian Processes (GPs), which are inherently probabilistic models. GPs provide both a prediction and an associated confidence interval (Rasmussen 2003), making them well-suited to scientific applications where uncertainty estimation is essential. They are particularly effective for modeling smooth trends and perform well on relatively small datasets. However, GPs also have limitations: they assume Gaussian-distributed data (which may not always hold for atmospheric turbulence) (Jones et al. 2004), and their computational cost scales poorly with increasing dataset size.

To overcome these limitations, we incorporate normalizing flows in our analysis. The FLOTS model is a generative and probabilistic deep learning approach that transforms a simple base distribution (e.g., Gaussian) into a complex target distribution through a sequence of invertible mappings (Papamakarios et al. 2021). This allows FLOTS to capture non-Gaussian characteristics

in the data while providing full probabilistic predictions. In addition, FLOTS scales more efficiently with dataset size than GPs, making it a promising candidate for high-resolution or operational turbulence forecasting.

In summary, this study compares three types of models for atmospheric seeing prediction:

- Deterministic deep learning models: RNN and LSTM.
- Probabilistic statistical model: Gaussian Processes (GP).
- Probabilistic deep learning model: Normalizing Flow (FLOTS).

We now describe the architecture and implementation details of each model we used in this analysis.

3.1. Recurrent Neural Network (RNN)

RNNs are a class of neural networks specifically designed to process sequential data by capturing temporal dependencies. Unlike traditional feedforward networks such as multilayer perceptrons, RNNs incorporate hidden states that enable information to persist across time steps. This is accomplished through a recursive structure, where the hidden state vector at time step t , denoted by h_t , is computed as

$$h_t = \sigma(W_h h_{t-1} + W_{\epsilon_-} \epsilon_{-,t} + b_h), \quad (1)$$

where $\epsilon_{-,t}$ is the input at time step t , h_{t-1} is the previous hidden state vector, W_h and W_{ϵ_-} are weight matrices, b_h is a bias term, and σ denotes a nonlinear activation function. In the encoder-decoder framework used in this work, h_t denotes the hidden state of the encoder RNN, which processes the input sequence and summarizes it into a latent representation.

The decoder then generates the forecast sequence using its own hidden state g_t , which is conditioned on the final encoder state h_T . The decoder state evolves as

$$g_t = \sigma(W_g g_{t-1} + W_c h_T + W_y \hat{\epsilon}_{t-1} + b_g), \quad (2)$$

where W_g , W_c , and W_y are weight matrices and b_g is a bias term. The term $\hat{\epsilon}_{t-1}$ denotes the predicted seeing value at the previous time step. This autoregressive dependency allows the decoder to propagate temporal information through the generated forecast sequence. The predicted seeing value at time step t is obtained by applying a linear projection to the decoder hidden state:

$$\hat{\epsilon}_{+,t} = W_{\epsilon_+} g_t + b_{\epsilon_+}. \quad (3)$$

In this study, RNNs were employed as an initial approach for modeling the temporal dynamics of atmospheric turbulence. The architecture consists of an encoder RNN layer with 100 hidden units, followed by two decoder RNN layers, each also comprising 100 hidden units, which further refine and propagate the encoded temporal information (Cho et al. 2014; Pascanu et al. 2014). To mitigate overfitting, a dropout layer with a rate of 0.3 is inserted between the encoder and decoder layers. The model is trained using the Mean Squared Error (MSE) loss function, defined as:

$$\mathcal{L}_{\text{MSE}} = \frac{1}{N} \sum_{i=1}^N (\epsilon_{+,i} - \hat{\epsilon}_{+,i})^2 \quad (4)$$

where $\epsilon_{+,i}$ and $\hat{\epsilon}_{+,i}$ represent the true and predicted seeing values, respectively. Optimization is performed using the Adam algorithm with an initial learning rate of 10^{-4} . A learning rate scheduler is employed to reduce the rate by a factor of 0.5 if the validation loss plateaus for five consecutive epochs. Although effective at capturing short-term dependencies, RNNs suffer from the vanishing gradient problem (Hochreiter 1998). During backpropagation through time (BPTT), the loss can be written as a sum over time steps, $\mathcal{L} = \sum_k \mathcal{L}_k$. The gradient of a future loss term with respect to a hidden state at an earlier time step t (with $k > t$) follows from the chain rule:

$$\frac{\partial \mathcal{L}_k}{\partial h_t} = \frac{\partial \mathcal{L}_k}{\partial h_k} \frac{\partial h_k}{\partial h_t}. \quad (5)$$

Because the hidden states are computed recursively, the term $\frac{\partial h_k}{\partial h_t}$ involves repeated multiplications of the recurrent weight matrix W_h . As a result, the gradient contains products of the form

$$\frac{\partial h_k}{\partial h_t} \propto \prod_{i=t+1}^k W_h. \quad (6)$$

If the spectral radius (largest eigenvalue) of W_h is smaller than one, these repeated multiplications cause the gradient to decay exponentially as $k - t$ increases, making it difficult for the network to learn long-term dependencies. This limitation is particularly detrimental when modeling sequences that require memory of distant past events. To address this issue, more advanced architectures such as Long Short-Term Memory (LSTM) networks introduce gating mechanisms that regulate the flow of information and mitigate gradient decay (Hochreiter & Schmidhuber 1997b). Accordingly, this study transitions to LSTM-based models to assess whether they provide tangible benefits over standard

Parameter	Details
Input Feature	1 (seeing values)
Hidden Units	100
Number of Layers (RNN/LSTM)	3 (1 encoder, 2 decoders)
Dropout Rate	0.3
Fully Connected Layer	Linear
Loss Function	MSE
Optimizer	Adam, learning rate=10 ⁻⁴
Batch Size	32
Epochs	100
Learning Rate Scheduler	Reduces learning rate by 50% if validation loss does not improve for 5 epochs

Table 1. Model Architectures and Hyperparameters for RNN and LSTM.

RNNs for seeing prediction, especially in the presence of long-range temporal dependencies.

3.2. Long Short-Term Memory (LSTM)

The LSTM model implemented in this study is designed to predict atmospheric seeing by capturing potential long-term dependencies in sequential turbulence data. LSTMs extend standard RNNs by addressing the vanishing gradient problem, which limits the ability of conventional RNNs to retain information over long sequences. By incorporating an internal gating mechanism, LSTMs regulate the flow of information, enabling the selective storage of relevant past data while discarding less useful details. This property makes them particularly suitable for time series forecasting, where dependencies between past and future observations may play a crucial role.

Unlike standard RNNs, which rely solely on recurrent connections, LSTMs introduce three gates (Eq. 7) that govern information flow. The following equations describe the operations of a single LSTM cell, which is used in both the encoder and decoder layers of the architecture. The forget gate determines the extent to which past information should be retained or discarded. The input gate controls how much new information is added to the internal memory, while the output gate regulates how much of the stored information contributes to the current hidden state. These mechanisms allow the model to dynamically adjust the influence of past observations, mitigating the issues associated with long-term dependencies in sequential data:

$$\begin{aligned}
 f_t &= \sigma(W_f[h_{t-1}, \epsilon_{-,t}] + b_f), \\
 i_t &= \sigma(W_i[h_{t-1}, \epsilon_{-,t}] + b_i), \\
 o_t &= \sigma(W_o[h_{t-1}, \epsilon_{-,t}] + b_o)
 \end{aligned}
 \tag{7}$$

where f_t, i_t, o_t represent the forget, input, and output gates, respectively; h_{t-1} is the hidden state from

the previous time step; $\epsilon_{-,t}$ is the input at time t ; and W_f, W_i, W_o and b_f, b_i, b_o are learnable weight matrices and bias terms. The sigmoid activation function $\sigma \in (0, 1)$ allows each gate to control the extent of information flow.

The cell state c_t , which stores long-term information, is updated using

$$\tilde{c}_t = \tanh(W_c[h_{t-1}, \epsilon_{-,t}] + b_c) \tag{8}$$

$$c_t = f_t \odot c_{t-1} + i_t \odot \tilde{c}_t \tag{9}$$

where \tilde{c}_t is the candidate cell state, c_{t-1} is the previous cell state, and \odot denotes element-wise multiplication.

The hidden state is then computed by modulating the updated cell state through the output gate:

$$h_t = o_t \odot \tanh(c_t) \tag{10}$$

where o_t is the output gate. This operation controls how much of the internal memory stored in the cell state contributes to the hidden representation passed to the next time step or subsequent network layers.

In the encoder–decoder architecture used in this study, the decoder is conditioned on the final encoder hidden state h_T , which summarizes the input sequence. The decoder LSTM follows the same gating structure as the encoder. However, instead of receiving the past seeing measurements $\epsilon_{-,t}$ as input, the decoder operates autoregressively and takes as input the previously generated prediction $\hat{\epsilon}_{+,t-1}$. Consequently, the decoder updates its internal states using the same LSTM equations, with the input $\hat{\epsilon}_{+,t-1}$ replacing $\epsilon_{-,t}$.

The decoder hidden state g_t is obtained from the decoder cell state d_t through

$$g_t = o_t \odot \tanh(d_t), \tag{11}$$

where o_t is the output gate of the decoder LSTM.

The predicted seeing value is obtained by applying a linear projection to the decoder hidden state:

$$\hat{\epsilon}_{+,t} = W_{\epsilon_+} g_t + b_{\epsilon_+} \tag{12}$$

While LSTMs are designed to capture long-term dependencies, it remains uncertain whether such dependencies are present in atmospheric seeing data. Therefore, their effectiveness relative to standard RNNs remains to be evaluated for this dataset.

The architecture of the LSTM model follows the same structure as the RNN model described previously, with LSTM layers replacing the standard RNN layers. The hyperparameters and optimization strategies, including batch size, learning rate, dropout rate, and loss function,

are consistent with those used for the RNN model and are summarized in Table 1.

3.3. Gaussian Process (GP)

GPs are employed in this study to predict atmospheric seeing, providing uncertainty estimates for the predictions. Unlike deterministic models, GPs are non-parametric probabilistic models that define a distribution over functions (Rasmussen 2003; Seeger 2004). Specifically, a GP assumes that any finite collection of inputs, the corresponding function values are jointly distributed according to a multivariate Gaussian distribution, enabling the model to produce both a predictive mean and an associated confidence interval at each new input. Formally, a GP is defined by a mean function $\mu(t)$ and a covariance function (kernel) $k(t, t')$, such that:

$$f(t) \sim \mathcal{GP}(\mu(t), k_\theta(t, t')) \quad (13)$$

where θ collects the kernel hyperparameters (length scale, signal variance, noise).

Let $\mathcal{D} = \{\epsilon_-^i, \epsilon_+^i\}_{i=1}^N$ denote the training dataset, where N is the total number of training samples, $\epsilon_-^i \in \mathbb{R}^{d_-}$ is the input seeing vector (for d_- time steps) and $\epsilon_+^i \in \mathbb{R}^{d_+}$ is the corresponding output values (for d_+ time steps). Under the GP prior, the key assumption is that the joint distribution of the input and output vectors can be modeled as a multivariate Gaussian distribution, with a covariance structure governed by a kernel function that encodes similarity between input points.

$$\begin{bmatrix} \epsilon_- \\ \epsilon_+ \end{bmatrix} \sim \mathcal{N} \left(\begin{bmatrix} \mu_- \\ \mu_+ \end{bmatrix}, \begin{bmatrix} K_{--} + \sigma_n^2 \mathbf{I} & K_{-+}^\top \\ K_{-+} & K_{++} \end{bmatrix} \right) \quad (14)$$

where, μ_- and μ_+ are the mean functions for the input and output values and

$$\begin{aligned} K_{--} &= k(t_-, t_-) \in \mathbb{R}^{d_- \times d_-} \\ K_{-+} &= k(t_+, t_-) \in \mathbb{R}^{d_+ \times d_-} \\ K_{++} &= k(t_+, t_+) \in \mathbb{R}^{d_+ \times d_+} \end{aligned} \quad (15)$$

Here, $k(t, t')$ denotes the kernel function, which determines the correlation between time steps t and t' . As before, t_- and t_+ denote time steps of the input and output, respectively. \mathbf{I} is the $d_- \times d_-$ identity matrix and σ_n^2 is the variance of the Gaussian observation noise, which accounts for measurement errors or stochastic fluctuations in the data.

The output seeing ϵ_+ given the input values ϵ_- therefore follows a conditional Gaussian distribution given by,

$$\epsilon_+ | \epsilon_- \sim \mathcal{N}(\boldsymbol{\mu}_{\epsilon_+|\epsilon_-}, \Sigma_{\epsilon_+|\epsilon_-}), \quad (16)$$

with

$$\begin{aligned} \boldsymbol{\mu}_{\epsilon_+|\epsilon_-} &= \boldsymbol{\mu}_+ + K_{-+} (K_{--} + \sigma_\epsilon^2 \mathbf{I})^{-1} (\epsilon_- - \boldsymbol{\mu}_-), \\ \Sigma_{\epsilon_+|\epsilon_-} &= K_{++} - K_{-+} (K_{--} + \sigma_\epsilon^2 \mathbf{I})^{-1} K_{-+}^\top. \end{aligned} \quad (17)$$

This formulation allows GPs to output both the predicted seeing value and an associated standard deviation that quantifies prediction uncertainty. In our study, we use the exponential kernel:

$$k_\theta(t, t') = \sigma^2 \exp\left(-\frac{|t - t'|}{l}\right), \quad (18)$$

where σ^2 is the variance, l is the length-scale. This kernel was selected for its ability to model the decaying temporal correlation present in turbulence data. When t and t' correspond to nearby time steps, the correlation between ϵ and ϵ' is high, and as the time difference increases, the correlation decays exponentially. To make GP training computationally manageable, a random subset of 500 (ϵ_-, ϵ_+) pairs was selected from the training set. During hyperparameter optimization, only the input sequences ϵ_- are used to fit the GP model, while the corresponding targets ϵ_+ are used later for evaluating the predictions. This choice balances computational cost and model accuracy, since computing the posterior involves inverting an $d_- \times d_-$ matrix at a cost of $\mathcal{O}(d_-^3)$. Using these batches, the GP learned its hyperparameters: length scale, variance, and noise variance. The length scale l controls the degree of temporal correlation between inputs, the signal variance σ^2 represents the amplitude of function variation, and the noise variance σ_n^2 accounts for measurement error. Hyperparameters learned across batches were averaged to ensure robust and stable behavior.

In our GP formulation (Eq. 13), the latent process $f(t)$ is defined by a mean function $\mu(t)$ and a covariance function $k_\theta(t, t')$, where the mean captures slow baseline variations and the kernel models correlated fluctuations around that baseline. This distinction is important because the GP is trained on many short seeing windows sampled throughout the year, which may exhibit different baseline seeing levels corresponding to different atmospheric regimes. Imposing a single fixed mean across all windows would therefore force the kernel to absorb these offsets and could bias the inferred hyperparameters. To avoid this, we apply per-window demeaning: for each window we subtract its empirical mean and fit a zero-mean GP to the residuals, adding back the window baseline at prediction time.

We also tested mean marginalisation by integrating out a constant offset under a flat prior and obtained nearly identical accuracy and uncertainty. This is expected in our setting because, over a few-hour window,

the mean is well approximated by a constant and forecasting is dominated by the kernel’s short-term correlation structure. While GPs provide a principled probabilistic framework for forecasting, their Gaussian assumptions and computational scaling may limit their flexibility for modeling complex turbulence dynamics. We therefore also investigate normalizing flows, a class of probabilistic deep learning models capable of representing more complex, non-Gaussian distributions.

3.4. Normalizing Flows (FLOTS)

Given samples from the target distribution $\epsilon \sim p(\epsilon)$, the normalizing flow learns a bijection map \mathbf{f} such that $\epsilon = \mathbf{f}_\phi(z)$, where z are samples from the latent Gaussian distribution and ϕ are the network weights to be optimized. Then, the target distribution can be mapped by a change of basis of the latent distribution,

$$p(\epsilon) \mapsto q_\phi(\epsilon) = n(\mathbf{f}_\phi^{-1}(\epsilon)) \left| \det \frac{\partial \mathbf{f}_\phi^{-1}}{\partial \epsilon}(\epsilon) \right|, \quad (19)$$

where \mathbf{f}_ϕ^{-1} is the inverse of \mathbf{f}_ϕ ($z = \mathbf{f}_\phi^{-1}(\epsilon)$) and $\partial \mathbf{f}_\phi^{-1} / \partial \epsilon$ is its corresponding Jacobian. A neural network models the invertible transformation \mathbf{f} which can be made arbitrarily expressive, limited only by the expressivity of the network. In theory, any target distribution $p(\epsilon)$ can be generated from the base distribution $n(z)$ under reasonable assumptions (Villani 2003; Bogachev et al. 2005; Medvedev 2008).

The normalizing flow parameters ϕ are optimized using the cross-entropy loss defined as,

$$\begin{aligned} L(\phi) &= - \int_{\mathbb{R}^d} p(\epsilon) \log(q_\phi(\epsilon)) d\epsilon \\ &= -\mathbb{E}_{p(\epsilon)} [\log(q_\phi(\epsilon))], \end{aligned} \quad (20)$$

where $\mathbb{E}_{p(\epsilon)}$ represents the expectation value for samples of $\epsilon \sim p(\epsilon)$. Thus, given a set of independent samples from the target distribution, the flow maximizes its predicted log-probability of the samples. The flow can be extended to learn a conditional probability distribution by passing the conditional information, often referred to as *context*, as input to the neural network.

Given observations of the seeing for past and future timesteps, $\{\epsilon_-, \epsilon_+\}$, we train a normalizing flow to model the probability distribution of future seeing values conditioned on past observations, $p(\epsilon_+ | \epsilon_-)$. The trained flow can then be used to produce predictions of future seeing values sampled from the conditional distribution i.e., $\hat{\epsilon}_+ \sim p(\epsilon_+ | \epsilon_-)$.

In this implementation, we use a class of normalizing flows called masked autoregressive flow (MAF, Papamakarios et al. (2017)). The MAF implementation of

NF expands $p(\epsilon)$ as the product of autoregressive conditional probabilities:

$$p(\epsilon_{d:1}) = p(\epsilon_d | \epsilon_{d-1:1}) \times p(\epsilon_{d-1} | \epsilon_{d-2:1}) \times \dots \times p(\epsilon_1), \quad (21)$$

where $\epsilon_{d:1}$ is the d -dimensional vector (first d time-steps). Conditioning on the past values ϵ_- , $p(\epsilon_{d:1} | \epsilon_-)$ is computed in MAF as:

$$\begin{aligned} p(\epsilon_{d:1} | \epsilon_-) &= p(\epsilon_{d+1} | \epsilon_{d-1:1}, \epsilon_-) \\ &\times p(\epsilon_{d+2} | \epsilon_{d-2:1}, \epsilon_-) \\ &\times \dots \times p(\epsilon_{d+1} | \epsilon_-). \end{aligned} \quad (22)$$

To this end, ϵ_- is passed to the MAF through a context encoder $\mathcal{C}(\epsilon_-) \in \mathbb{R}^{2d+}$ to identify the d_+ -dimensional mean and standard deviation of the normal distribution in the latent space, i.e., $z \sim n_{\mathcal{C}(\epsilon_-)}(z)$, where $n_{\mathcal{C}(\epsilon_-)} := \mathcal{N}(\mathcal{C}_{d:1}(\epsilon_-), \mathcal{C}_{2d:d+1}(\epsilon_-))$. The flow models the transformation \mathbf{f}_ϕ that satisfies $\epsilon_+ = \mathbf{f}_\phi(z)$, and approximates $p(\epsilon_+ | \epsilon_-)$ by $q_\phi(\epsilon_+ | \epsilon_-)$:

$$\begin{aligned} p(\epsilon_+ | \epsilon_-) &\mapsto q_\phi(\epsilon_+ | \epsilon_-) \\ &= n_{\mathcal{C}(\epsilon_-)}(\mathbf{f}_\phi^{-1}(\epsilon_+)) \left| \det \frac{\partial \mathbf{f}_\phi^{-1}}{\partial \epsilon_+}(\epsilon_+) \right|. \end{aligned} \quad (23)$$

The encoder \mathcal{C} can be any tunable function of ϵ_- whose parameters are trained along with the MAF by the optimizer. We find the best results with an LSTM encoder, outperforming other variants we explored, including a simple linear network, a fully connected network (FCN), an RNN, and a GP.

3.5. Hyperparameter tuning

An essential step in training our ML algorithms involved determining the optimal hyperparameters that describe the model. In the case of neural network architectures, the hyperparameters include the number and shapes of the layers of the network. For GPs, these correspond to the choice of kernels and their parameters. Another important common hyperparameter is the model-specific training length to achieve the best predictions for the 2-hour forecast. We select the optimal hyperparameters based on empirical performance. To assess the accuracy of these predictions, we evaluated various error metrics, including Root Mean Square Error (RMSE) and the Pearson correlation coefficient (r). In these equations, N represents the sample size, while X_i and Y_i denote the predicted values from the ML models and the corresponding measurements, respectively. \bar{X} and \bar{Y} are the means of the variables X and Y .

Figure 1 compares model performance by computing the RMSE between the predicted seeing values ($\hat{\epsilon}_+$)

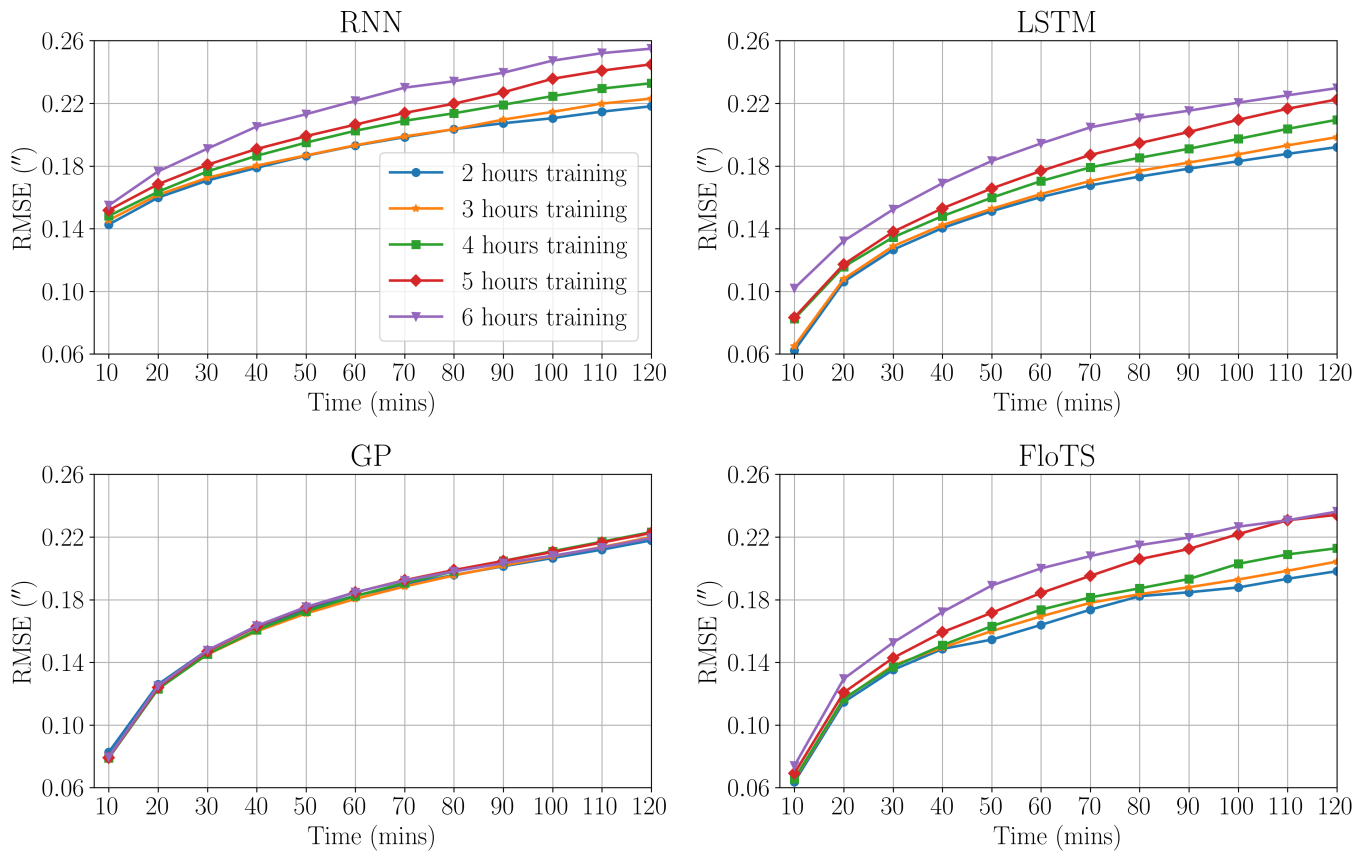


Figure 1. RMSE for each training duration: 2 hours (blue), 3 hours (orange), 4 hours (green), 5 hours (red), and 6 hours (purple), evaluated over a fixed 2-hour prediction window. Results are shown for all models: RNN, LSTM, GP, and FLOTS (FLOW).

and the observations (ϵ_+) across different historical data lengths (2, 3, 4, 5, and 6 hours) for a 2-hour prediction. As expected, the RMSE increases with prediction horizon across all models due to growing uncertainty and the weaker influence of initial conditions. While longer histories can be beneficial, their utility depends on the temporal correlation length, short correlation lengths limit the contribution of earlier observations. Moreover, the ability to leverage longer histories effectively is also shaped by network training efficiency and kernel choice.

A clear trend is observed for the RNN, LSTM, and FLOTS models: as the historical data length decreases, the RMSE also decreases, with the best performance achieved for the 2-hour historical data. This could be explained as shorter historical data lengths limiting the complexity of the temporal relationships the model must learn, reducing overfitting, and improving its ability to generalize. Additionally, shorter input windows align more closely with the 2-hour prediction target, allowing the model to focus on the most relevant temporal patterns without being influenced by distant, less impactful data points. That said, using longer historical windows does not degrade performance by much; the RMSE

curves remain consistent across training lengths and still show a clear decrease as the input window shortens. We therefore retain the 2-hour window as the default, as it yields the lowest RMSE while keeping the input compact and well matched to the prediction horizon.

For the GP model, varying the historical data length does not significantly affect prediction performance, as shown in Figure 1 by the overlapping curves for all input lengths. This behavior can be attributed to the nature of the Gaussian Process formulation and its kernel. Once the hyperparameters are learned, the GP relies on the kernel function to model temporal correlations between observations. In practice, this means that predictions are primarily influenced by data points that lie within the kernel’s effective correlation length. As a result, increasing the amount of historical data beyond this correlation range does not significantly affect the predictions. The GP becomes relatively insensitive to the total length of the input window, since distant observations contribute very little to the prediction due to their low covariance. Consequently, even when trained on different durations of data, the GP produces nearly identical performance for a fixed prediction horizon, as

it effectively exploits only the most relevant, locally correlated information.

Consequently, to maintain consistency across models, we selected a 2-hour training window as the optimal choice for the 2-hour prediction horizon. This training duration was also adopted in the studies by Milli et al. (2019), Turchi et al. (2022), and Masciadri et al. (2023).

3.6. Calibration of Probability Distributions

Ideally, in the limit of infinite data samples, expressivity, and computational resources, normalizing flows can accurately model probability distributions. Likewise, assuming Gaussianity, GPs can also correctly model the distribution. However, in practice, due to the finite amount of data and limited expressivity of the network/kernel, discrepancies may arise between the model approximation and the true underlying distribution. Since normalizing flows and GPs are density estimators that enable rapid sample generation and corresponding probability estimation, it is feasible to efficiently evaluate the quality of the predicted distribution and apply fine corrections through calibration.

The coverage is the probability with which a credible or confidence region contains the observed value across multiple realizations of the dataset. A parameter region with credibility a is a subset of the parameter space wherein the true value lies with a probability a . We define the credible region using the highest posterior density (HPD), which by construction is the smallest region with this credible probability. To compute the credible regions, we compute the inverse cumulative distribution function (F^{-1}) from the samples, in descending order of probability density. The nominal coverage (i.e., the HPD credible region) at level a_0 is the set of ϵ_+ values for which $p(\epsilon_+|\epsilon_-)$ is greater than or equal to the threshold $p(F^{-1}(a_0))$, such that the cumulative posterior mass does not exceed a_0 . The empirical coverage is the proportion of times the true value falls within this credible region of the corresponding expected, nominal coverage. A well-calibrated density estimator will have matching empirical and nominal coverages.

Building on the calibration prescription of Srinivasan et al. (2025), a generalization of the temperature scaling in Guo et al. (2017), we look at the mismatch between the empirical and nominal coverage to characterize the fidelity of the modeled probability distribution with that of the data samples. To illustrate the potential mismatch, we use a probability-probability (PP) plot, as illustrated in Figure 2, which displays the empirical coverage as a function of the nominal credibility levels. A perfectly calibrated model yields a diagonal 45° line due to the perfect agreement between expected and nomi-

nal coverage. Deviations above (below) this line reveal under(over)-confidence in the predictive distributions as illustrated in Figure 2.

As depicted in Figure 2, in the likely scenario of under- or over-confident empirical coverage for different values of the nominal coverage, we apply a temperature-based calibration technique shown below,

$$p^*(\epsilon_+|\epsilon_-) = p(\epsilon_+|\epsilon_-)^{1/\mathbf{T}^*(a)}, \quad (24)$$

where $p^*(\epsilon_+|\epsilon_-)$ and $p(\epsilon_+|\epsilon_-)$ are the calibrated and uncalibrated probability distributions respectively. \mathbf{T}^* is the calibration temperature vector as a function of the nominal coverage \mathbf{a} and which minimizes the mean square difference between the ideal PP plot (45° line) and that computed by scaling the uncalibrated probability density. For a given nominal coverage a_0 , if the empirical coverage is under-confident ($> a_0$), the corresponding calibration temperature $\mathbf{T}^*(a_0) < 1$ to contract the distributions. Conversely, if the empirical coverage is over-confident ($< a_0$), $\mathbf{T}^*(a_0) > 1$ to expand the distributions. A perfectly calibrated distribution will have $\mathbf{T}^*(a) = 1$.

For our current analysis, we find adequate calibration when approximating \mathbf{T}^* as a bi-quadratic function of the nominal coverage given by

$$\mathbf{T}^*(\mathbf{a}) = T_5\mathbf{a}^4 + T_4\mathbf{a}^3 + T_3\mathbf{a}^2 + T_2\mathbf{a} + T_1, \quad (25)$$

where T_1, T_2, T_3, T_4, T_5 are fitting coefficients that minimize the mean square difference between the ideal and uncalibrated PP plots, computed using a stochastic gradient descent algorithm.

In practice, we produce samples (i.e., predictions) from a calibrated distribution by importance-weighted resampling of the uncalibrated samples with weights given by the ratio of the calibrated and uncalibrated probability densities described in Eq. 24.

We present the uncalibrated and calibrated PP plots for FLOTS and GP in Figures 3 and 4, respectively. Notably, for the GP, the calibrated curve remains significantly offset from the ideal 45° line, indicating a mismatch between the assumed Gaussian predictive distribution and the empirical distribution of the seeing. To address this, we investigate a more flexible, nonparametric temperature parameterization in Appendix A. Nevertheless, even with this increased flexibility, achieving alignment with the ideal calibration curve remains challenging.

4. RESULTS

Figure 5 compares the performance of all models trained using a 2-hour input duration. The left and

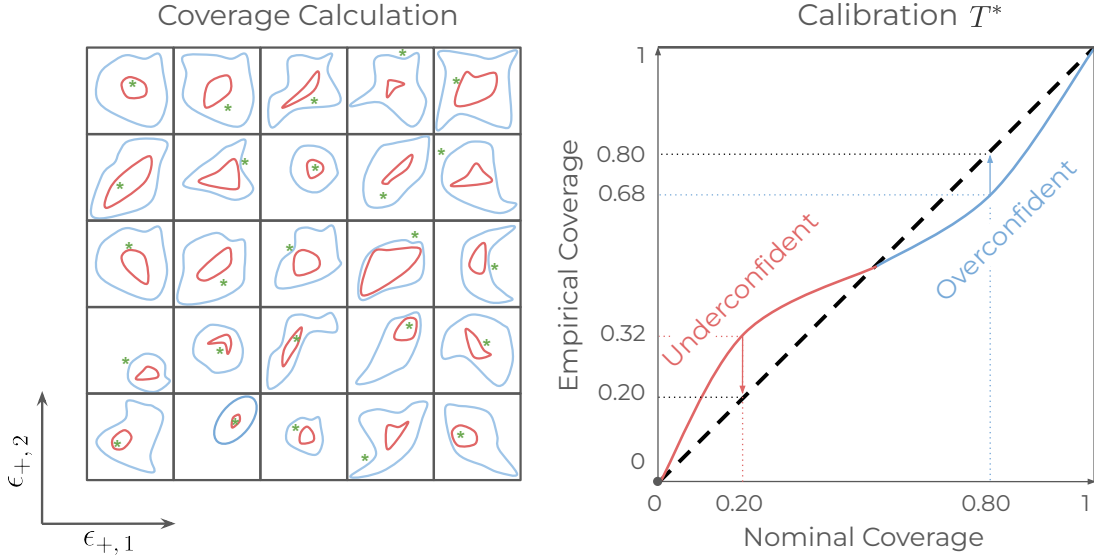


Figure 2. Illustration of the calculation and calibration of the coverage for an example: predictions for +10 and ± 20 minutes. **Left:** examples of different observations (green star) and the corresponding predicted probability distribution shown by two contours of nominal coverage 0.2 (inner, red) and 0.80 (outer, blue). **Right:** the corresponding uncalibrated PP-plot of the empirical vs nominal coverage. The dashed black diagonal line is the ideal coverage, and the red (blue) curve represents under-(over) confident regions. The two figures together illustrate that the contours of nominal coverage 0.2 (0.80) have an empirical coverage of 0.32 (0.68), indicating under-(over) confidence. The ideal calibration temperature vector, a function of the nominal coverage, contracts (expands) the probability density of under-(over) confident regions in the parameter space.

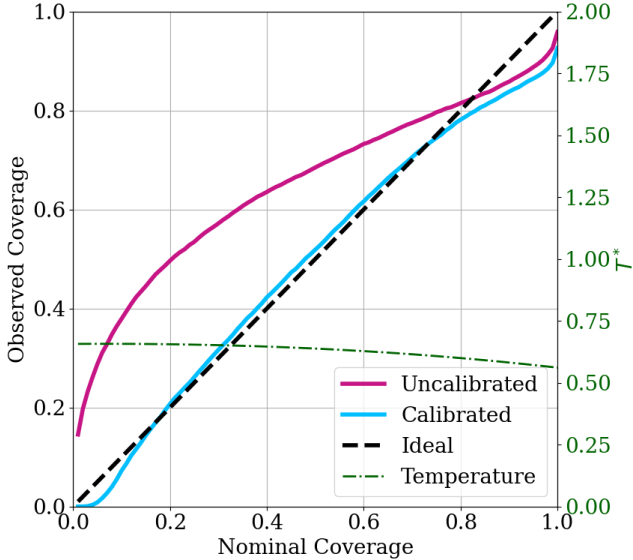


Figure 3. Comparison of the PP plots from the uncalibrated (purple) and calibrated (blue) FLOTS predictions. The 45° black dashed line represents the ideal coverage. The green dot-dashed line, which corresponds to the secondary y-axis, shows the optimal temperature as a function of nominal coverage. The calibration temperature is parameterized according to Equation 25.

right panels respectively display the RMSE and the Pearson correlation coefficient between predicted ($\hat{\epsilon}_+$) and observed (ϵ_+) seeing values as functions of forecast lead time, for the four models: RNN, LSTM, GP,

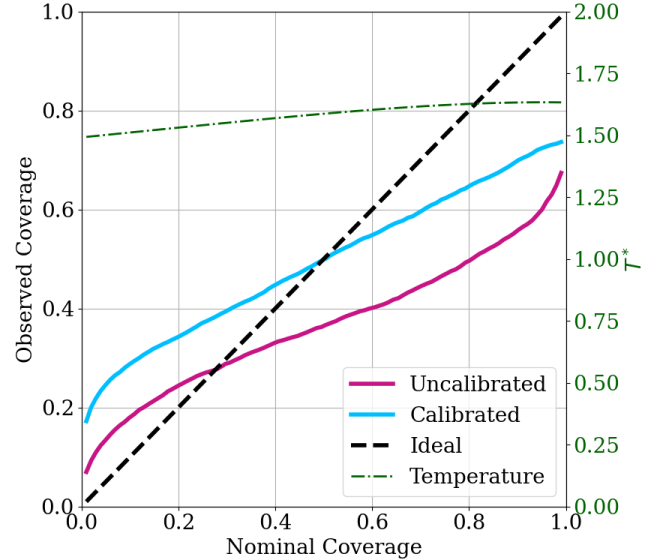


Figure 4. Same as Figure 3 for GP predictions. An alternative calibration is presented in Appendix A.

and FLOTS. Across the two metrics, we observe a consistent trend: model performance deteriorates as the prediction horizon increases. This is evidenced by increasing RMSE along with declining correlation coefficients. These two metrics capture complementary aspects of forecast quality. RMSE quantifies the average magnitude of prediction errors in the same physical units as the target variable, in this case, arcseconds

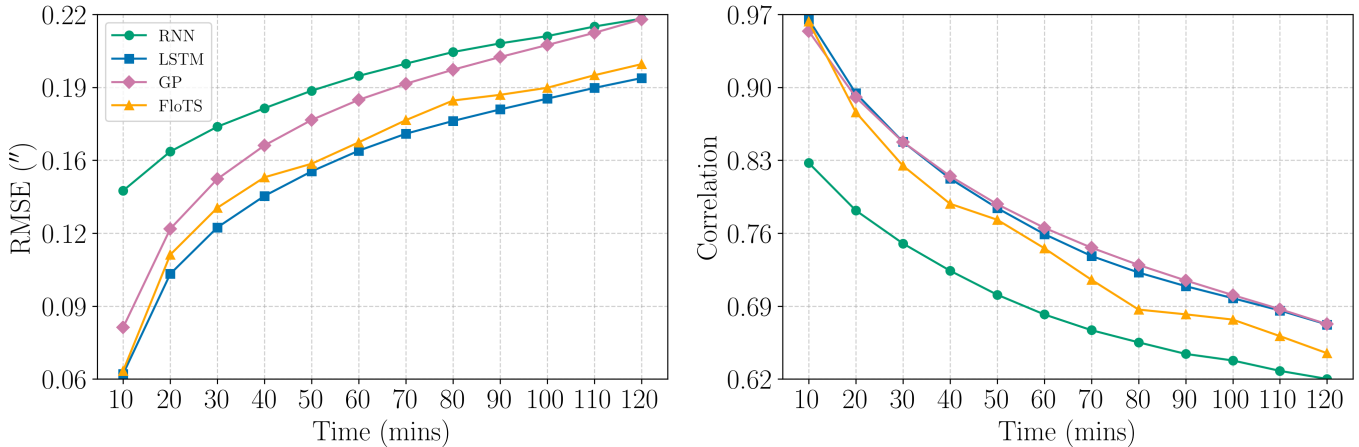


Figure 5. Forecasting performance of all models trained using a 2-hour input window. **Left:** RMSE, and **Right:** Pearson correlation coefficient, both computed between the predicted and observed seeing values and plotted as a function of forecast lead time.

of seeing, penalizing larger deviations more heavily due to its quadratic nature. A lower RMSE indicates that the model is making more accurate point forecasts on average, with fewer large errors.

In contrast, the Pearson correlation coefficient measures the linear association between predicted and true values, independently of their absolute scale. It captures how well the model predicts the direction and relative changes of the target variable. A high correlation implies that the model effectively tracks the trends and temporal structure of the signal, even if the amplitude is imperfectly predicted. Thus, combining RMSE and correlation gives a fuller picture: good predictions should not only be close in magnitude to the true values but should also follow their variations over time.

In Figure 5, left, we show that by the 2-hour mark, RMSE values reach approximately $0.20''$ for both LSTM and FLoTS, and around $0.22''$ for GP and RNN. These results indicate that LSTM and FLoTS achieve substantially lower errors on average. On the right, the correlation coefficients show that LSTM and GP maintain the strongest correlations with the ground truth across most of the forecast window, with FLoTS close behind, and RNN trailing in both metrics. These results underscore the superior short-term predictive capabilities of LSTM, FLoTS, and GP models, especially during the early stages of the forecast horizon. The LSTM benefits from its gated architecture, which allows it to selectively retain useful temporal information and mitigate the effects of noise. The FLoTS model performs similarly well, due to its probabilistic and non-linear modeling capacity, which captures both the mean behavior and the uncertainty structure of the data. The GP slightly underperforms, suggesting that a Gaussian approximation does not fully capture the distribution of seeing values.

In summary, the combination of low RMSE and high correlation for LSTM, FLoTS, and GP indicates both precise and trend-consistent predictions. RNN, on the other hand, lags in both respects, confirming its limited capacity to model complex temporal dependencies. While the LSTM achieves the lowest point-prediction errors overall, and the GP offers strong short-term accuracy grounded in a well-defined statistical framework, the FLoTS model is motivated by a different yet practically crucial criterion: the ability to deliver uncertainty estimates beyond point forecasts.

Standard LSTM inference typically provides a single prediction, whereas both GP and FLoTS produce probabilistic forecasts. However, the nature of this probabilistic output differs substantially. A GP yields a predictive distribution that is Gaussian, typically summarised by a mean and variance. This is a powerful and principled choice, but it also imposes a specific distributional shape. In practice, real-world time series often exhibit departures from Gaussianity. In contrast, the flow-based formulation underlying FLoTS learns a flexible conditional distribution directly from data. This allows it to represent non-Gaussian predictive shapes that vary across regimes, while remaining competitive in point accuracy. As a result, FLoTS provides a richer and potentially more realistic quantification of uncertainty, making it particularly valuable for applications where probabilities are as important as average error.

To further illustrate the advantages of the FLoTS model, especially its ability to characterize predictive uncertainty, we present below a case study. There, we visualize the predicted density from the FLoTS model alongside the point forecasts of other models and the confidence intervals of the GP. This allows for a more intuitive appreciation of the FLoTS model’s strengths

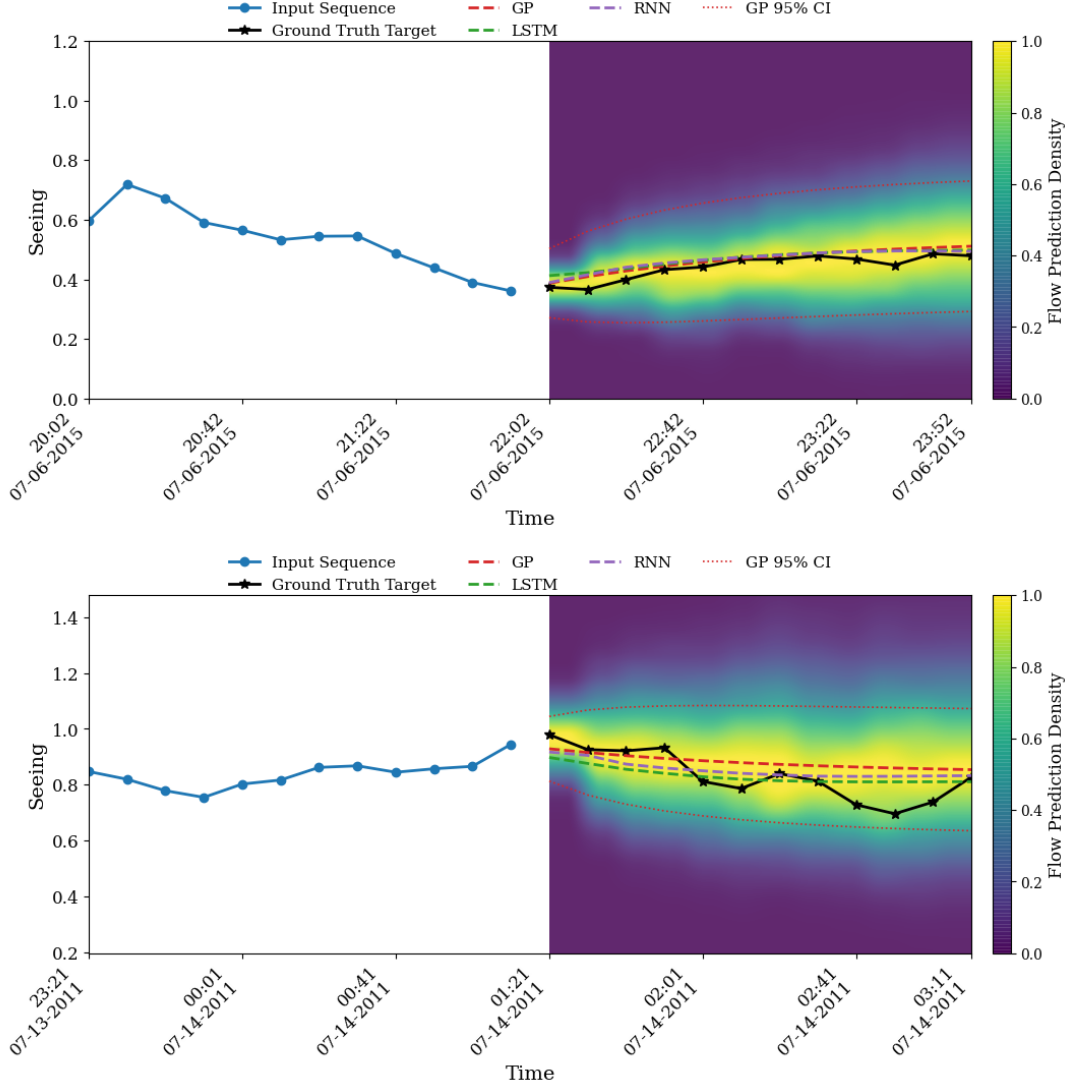


Figure 6. Comparison of the seeing predictions for two example nights: (top) 06 July 2015 and (bottom) 13 July 2011. The left side of each panel shows the input sequence (blue) used for forecasting. The right side displays the forecast horizon, including the ground truth (black), and predictions from multiple models: GP (red), RNN (purple), and LSTM (green). The heatmap represents the probability density predicted by FLOTS. For ease of representation, we scale the probability density by the maximum and minimum densities within each timestep. The 95% confidence interval of the GP is shown with small red dotted lines.

in capturing both accuracy and uncertainty. For these reasons, we consider the FLOTS model to be the most informative and robust overall.

CASE STUDY

To complement the quantitative evaluation, we present two case studies to qualitatively examine the behavior of different forecasting models on representative examples. These case studies provide a more comprehensible comparison of model outputs, particularly regarding the uncertainty captured by the probabilistic flow-based predictions and the GP.

Figure 6 shows the prediction results for the nights of 06 July 2015 and 13 July 2011. In both panels, the left side displays the input time series used for forecasting (in blue), while the right side shows the forecast horizon. The colored heatmap represents the probability density predicted by the normalizing flow model, estimated from 5000 posterior samples. Brighter regions indicate higher likelihood regions for the predicted seeing values. Notably, in both examples, the ground truth values (black line) fall within regions of high flow density, confirming that the flow model assigns high probability to the true future behavior. This alignment demonstrates the model’s ability to generate calibrated and informative

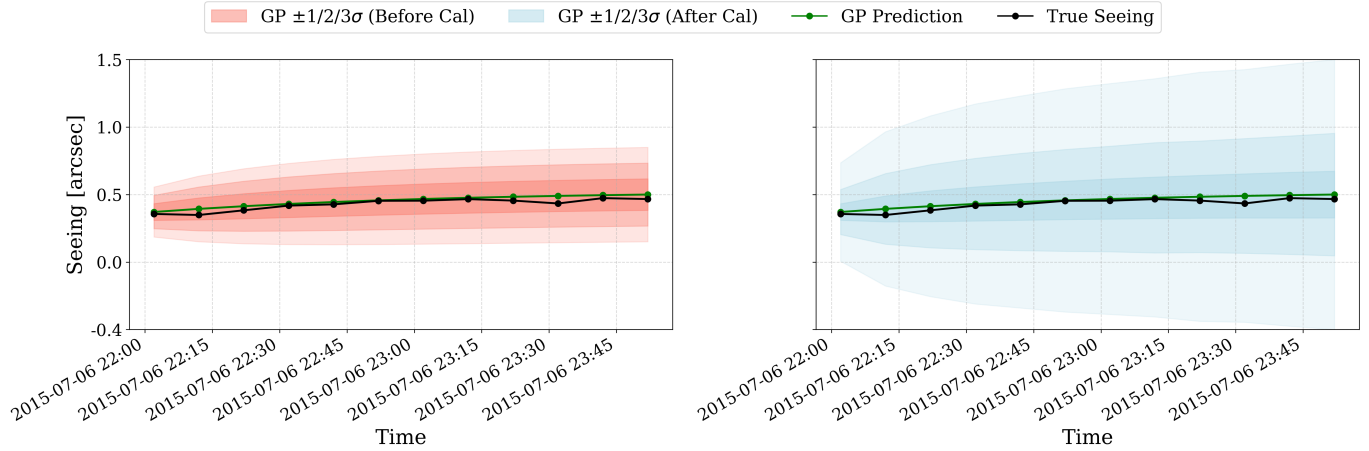


Figure 7. Left: GP predictive mean and uncertainty bounds over a 2-hour interval before posterior calibration for the case study of 06 July 2015. The shaded red regions indicate the 1σ , 2σ , and 3σ confidence intervals around the GP prediction. **Right:** Same prediction interval after applying posterior calibration, with blue shaded areas denoting the updated calibrated uncertainty bands. In both panels, the green line represents the GP predictive mean, and the black dots indicate the true seeing measurements.

forecasts, capturing not only the central trajectory but also the associated uncertainty. Alongside the FLOTS results, we show forecasts from the LSTM and RNN models, as well as the GP model, which provides both mean predictions and a 95% confidence interval under a Gaussian assumption.

In Figure 6, top, all three models generally follow the overall trend of the ground truth. Importantly, their predicted trajectories tend to pass through regions of moderate to high probability density in the flow, suggesting that the point forecasts are broadly consistent with the structure learned by the probabilistic model. The GP confidence interval (small red dotted lines) covers nearly all regions where the flow assigns non-negligible probability mass, that is, where the heatmap retains visible density. This reflects a strong agreement between the GP’s uncertainty estimates and the flow’s predictive distribution.

Figure 6, bottom, presents the second case study. Here again, the normalizing flow model successfully captures the trend and assigns high probability along the ground truth trajectory. Although the prediction is expressed as a distribution, the trend remains visually apparent in the density structure. The LSTM and RNN models produce forecasts that follow the general trend but remain relatively flat and closely aligned. This behavior likely results from the model’s limited ability to retain long-range temporal dependencies, combined with a regularizing tendency to revert to the training mean when the input sequence lacks strong predictive signals. The GP forecast appears relatively flat in the main plot because only the posterior mean is displayed. To provide a more comprehensive view of the predictive

uncertainty, we show posterior predictive plots of the GP model in Appendix Figure 10, illustrating the full predictive density of the forecasts.

To further highlight the importance of calibration for probabilistic forecasting, we show for the 06 July 2015 case study both the GP and FLOTS before and after calibration (Figures 7 and 8). In Figure 7, the calibration, by construction, leaves the GP predictive mean unchanged and still closely aligned with the observed seeing. The main impact of calibration is on the dispersion: after calibration (Figure 7, right), the $\pm 1\sigma$, $\pm 2\sigma$, and $\pm 3\sigma$ bands all increase, most noticeably at longer lead times, yielding more conservative uncertainty estimates. The widening is particularly pronounced for the $\pm 2\sigma$ and $\pm 3\sigma$ intervals relative to the $\pm 1\sigma$ band, which is consistent with the presence of non-Gaussian tails (positive kurtosis) in the seeing distribution. This behavior follows from the conclusions of Figure 4 that the uncalibrated GP was over-confident (under-dispersed), and that calibration corrects this by rescaling its predictive variance.

Figure 8 shows the corresponding uncalibrated (top) and calibrated (bottom) predictions for FLOTS. In each row, the blue line of the left panel shows the conditioning input sequence, while the right panel illustrates the forecast horizon as a predictive density color-map, overlaid with the ground-truth target in black, along with the point forecasts from GP/LSTM/RNN (see legend). Comparing the top and bottom plots in Figure 8, calibration changes the shape of the predictive distribution rather than its central tendency: probability mass is redistributed across the density, so that the ground-truth trajectory lies in regions of higher pre-

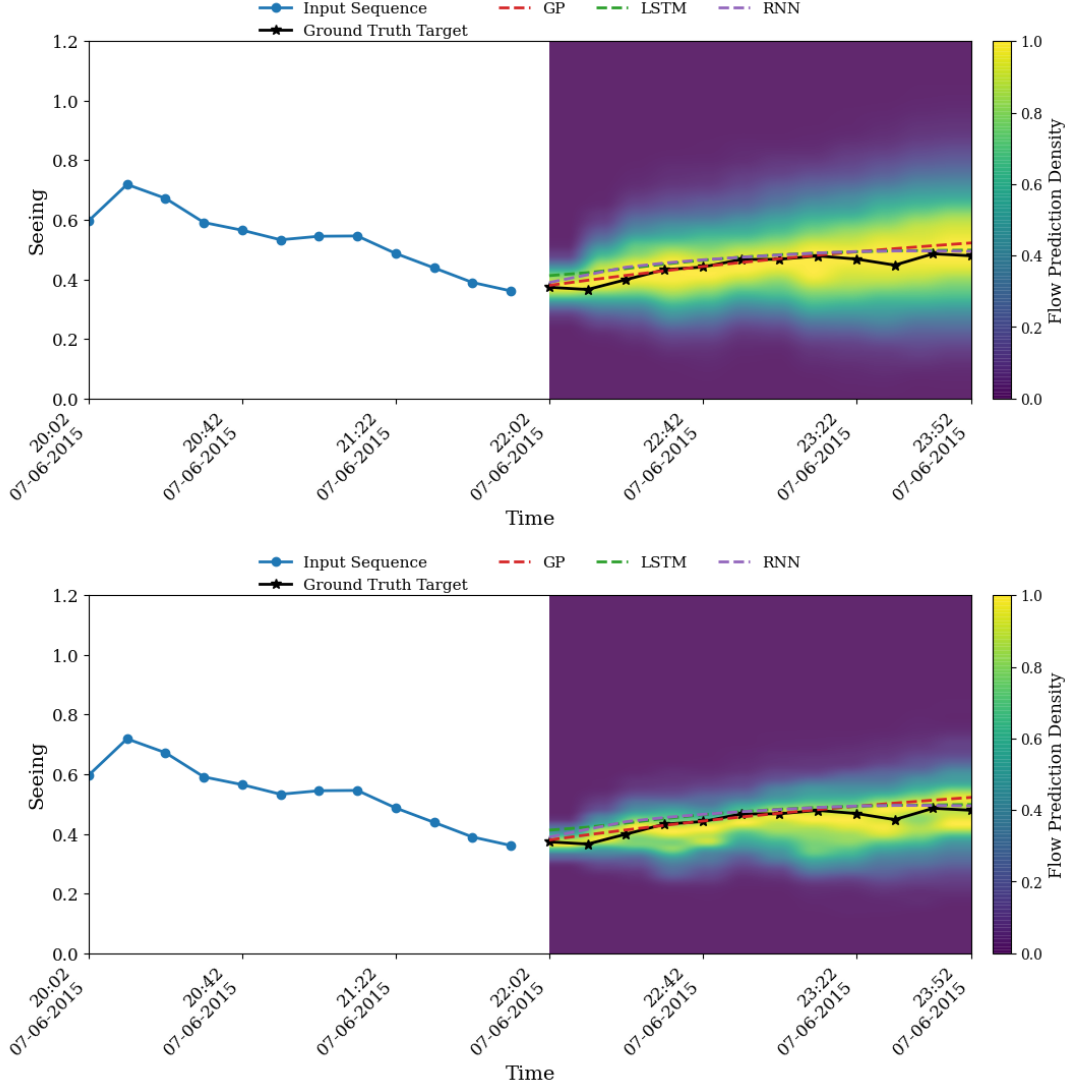


Figure 8. Comparison of the seeing prediction (a) before calibration and (b) after calibration for an example observation on 06 July 2015. The left side of each panel shows the input sequence (blue) used for forecasting. The right side displays the forecast horizon, including the ground truth (black), and predictions from multiple models: GP (red), RNN (purple), and LSTM (green). The heatmap represents the probability density predicted by FLOTS. For ease of representation, we scale the probability density by the maximum and minimum densities within each timestep.

dicted likelihood. In this example, calibration reduces excess probability and concentrates mass around the observed evolution, indicating that the uncalibrated flow was under-confident (over-dispersed). Overall, unlike the GP, where calibration primarily adjusts the dispersion of the predictive intervals, in FLOTS the calibration can also modify non-Gaussian features of the predictive distribution. As observed in the GP coverage results, the correction is not uniform across credibility levels: the higher-confidence intervals expand more than the $\pm 1\sigma$ region, indicating non-Gaussian behaviour in the data. In contrast, the calibration of FLOTS can reshape the predictive distribution itself, improving the reliability of

its uncertainty quantification without affecting the point prediction.

Together, these case studies demonstrate the advantages of FLOTS probabilistic modeling for capturing both the trajectory and the uncertainty of future seeing values. While RNN and LSTM models yield reasonable point forecasts, the GP and FLOTS models provide a more informative representation by producing full predictive distributions, thereby allowing uncertainty quantification.

5. CONCLUSIONS AND DISCUSSION

The objective of this study was to develop an accessible and effective method for short-term seeing predic-

tion, with practical applications in astronomical observation and optical communication. We aim to forecast seeing conditions up to 2 hours ahead, using MKWC historical data. To this end, we evaluated four models: a statistical model, GP, and three deep learning approaches, RNN, LSTM, and a normalizing flow-based model. A key distinguishing feature of our work compared to previous studies is the integration of probabilistic models, specifically GP and FLOTS, that not only provide deterministic forecasts but also quantify predictive uncertainty. This capability is particularly valuable for decision-making processes where understanding the confidence level of predictions is essential, for example in telescope scheduling.

Our experiments revealed that a 2-hour training window was optimal for all models, suggesting that seeing does not exhibit long-term temporal dependencies under the considered conditions. With this optimal context length, all four models produced reasonable forecasts, exhibiting the expected trend: increasing RMSE with forecasting horizon, while correlation with ground truth progressively decreases. Among the models, LSTM achieved the lowest errors overall, slightly outperforming the others in terms of point prediction accuracy. However, when considering both accuracy and uncertainty quantification, the FLOTS model offers the most favorable trade-off between precision and informativeness. As shown in the error and correlation metrics, its performance is very close to that of LSTM. Importantly, the case studies demonstrate that the FLOTS model’s predictive density not only captures the general trends of the ground truth but also tracks local variations, such as short-term increases and decreases in seeing values, with higher fidelity. This capacity to model both global behavior and fine-grained fluctuations enhances the realism of the predictions, making them more consistent with the observed data. In contrast, the GP kernels used in this study rely on very few parameters, and the specific kernel choices we adopted do not permit modeling multiple time scales in the predictive probability structure. This contrasts with FLOTS, which leverages a high-capacity architecture with many parameters and no such restriction. It is important to note, however, that this limitation is not intrinsic to GPs themselves, but rather a consequence of our decision to favor simple kernel formulations in this work. We also aim to explore more expressive GP kernels that can capture multi-scale temporal structures while preserving the interpretability and calibration advantages of the GP framework.

Such probabilistic forecasting makes the FLOTS model particularly well-suited for operational scenarios that demand not only accurate forecasts but also ro-

bust non-Gaussian uncertainty quantification to inform decision-making and risk assessment. The GP model follows closely, providing well-calibrated uncertainty estimates through a more rigid and less data-adaptive structure. An important observation is that the predictions from the LSTM and RNN consistently fall within the high-probability regions of the GP and FLOTS predicted densities, reinforcing the reliability of their uncertainty estimates. Furthermore, the 95% confidence intervals of the GP model consistently enclose the peaks where the FLOTS model maintains moderate to high confidence, emphasizing the complementary nature of these two probabilistic approaches. These results also highlighted the importance of calibration for probabilistic forecasts, especially for FLOTS, whose predictive distribution is inherently non-Gaussian. This leads to more reliable and trustworthy predictions.

In future work, we aim to investigate the incorporation of additional meteorological features, such as temperature, wind speed and direction, humidity, and atmospheric pressure, which are known to influence optical turbulence. While these variables may provide useful contextual information, their actual contribution to model performance remains to be evaluated. Feature engineering and selection will be necessary to determine whether these additional inputs enhance the predictive accuracy or simply add noise to the system (Dong & Liu 2018). Beyond the recurrent baselines considered in this thesis, self-attention-based Transformer (Wolf et al. 2020) architectures could be explored as an alternative sequence model. In contrast to RNNs/LSTMs, which compress past information into a fixed-size hidden state, Transformers form predictions by weighting past time steps through attention. This mechanism may be advantageous for seeing time series where the relevant temporal dependencies are not strictly local and may occur at multiple, potentially irregular, time scales. More generally, other generative architectures such as conditional variational autoencoders (VAEs) could also be considered for probabilistic forecasting, as they learn a conditional latent representation of the future given past observations (Doersch 2016). Furthermore, future research could explore ensemble strategies that leverage the strengths of different models, for instance, combining the LSTM’s deterministic forecasting capabilities with the FLOTS model’s probabilistic uncertainty quantification. These extensions would move toward a more comprehensive and operationally useful forecasting framework, capable of delivering both accurate predictions and confidence estimates, while also accounting for physical drivers of seeing variability.

ACKNOWLEDGEMENTS

The authors thank the Maunakea Weather Center (MKWC), particularly Dr. Steven Businger, Dr. Tiziana Cherubini, and Ryan Lyman, for providing essential atmospheric data that supported this study. We also acknowledge the Seeing Monitor Group for their efforts in maintaining and providing access to seeing measurements. Additionally, we extend our appreciation to the Canada-France-Hawaii Telescope (CFHT) staff for their operational support in maintaining the instruments and database that contributed to the see-

ing observations. RS acknowledges support from the European Union’s Horizon ERC Synergy Grant “Making Sense of the Unexpected in the Gravitational-Wave Sky” (Grant No. GWSky-101167314). Computational work has been partly made possible through SISSA-CINECA and CINECA-INFN agreements providing access to resources on LEONARDO at CINECA.MB. We gratefully acknowledge funding from the Centre National d’Études Spatiales (CNES) and the Université Côte d’Azur (UCA). This work was also supported by the French government through the UCAJEDI “Investments in the Future” program, managed by the National Research Agency (ANR) under grant ANR-15-IDEX-01.

APPENDIX

A. PIECEWISE LINEAR CALIBRATION

In addition to the smoothly varying polynomial parameterization of the temperature as a function of nominal coverage shown in Equation 25, we also consider a non-smooth alternative based on a piecewise-linear representation with the same number of free parameters. This formulation enables flexible localized adjustments of the calibration curve. Specifically, the function $\mathbf{T}^*(\mathbf{a})$ is defined as a piecewise-linear interpolation between five learnable anchor temperatures T_k at fixed uniformly spaced nodes,

$$\mathbf{T}^*(\mathbf{a}) = \begin{cases} T_1 + \frac{T_2 - T_1}{0.25}(a), & a \in [0, 0.25), \\ T_2 + \frac{T_3 - T_2}{0.25}(a - 0.25), & a \in [0.25, 0.5), \\ T_3 + \frac{T_4 - T_3}{0.25}(a - 0.5), & a \in [0.5, 0.75), \\ T_4 + \frac{T_5 - T_4}{0.25}(a - 0.75), & a \in [0.75, 1]. \end{cases} \quad (\text{A1})$$

In Figure 9, we present the piecewise-linear calibration of the GP. Compared to Figure 4, this approach yields a modest improvement in median coverage. However, as with the polynomial calibration, discrepancies persist at both low and high nominal coverage levels, and exact calibration is not achieved. This further underscores the limitation of the Gaussian assumption in GP models for describing the underlying seeing distribution, and explains the better calibration performance of the flow model shown in Figure 3.

B. POSTERIOR PREDICTIVE DISTRIBUTIONS FROM GP

Figure 10 presents the uncalibrated posterior predictive distributions for the same case studies discussed in Section 4, illustrating the uncertainty representation of the GP model. In both figures, the red dashed line represents the posterior mean, while the small red dotted lines denote the 95% confidence interval (CI). The probability density is estimated from 5000 posterior samples, each corresponding to a plausible future realization consistent with the model’s learned distribution.

As expected under the GP’s Gaussian assumptions, the majority of these samples (approximately 95%) lie within the 95% CI, confirming that the model’s uncertainty estimates are statistically well calibrated.

The corresponding probability density therefore appears smooth and relatively uniform, reflecting the Gaussian structure imposed by the GP. In contrast to the FLOTS, the density map does not exhibit strong local variations or fine-scale structures, as the predictive distribution is fully determined by its mean and covariance. This behavior highlights the FLOTS model’s ability to capture complex, data-driven uncertainty structures that extend beyond the constraints of Gaussian-based models.

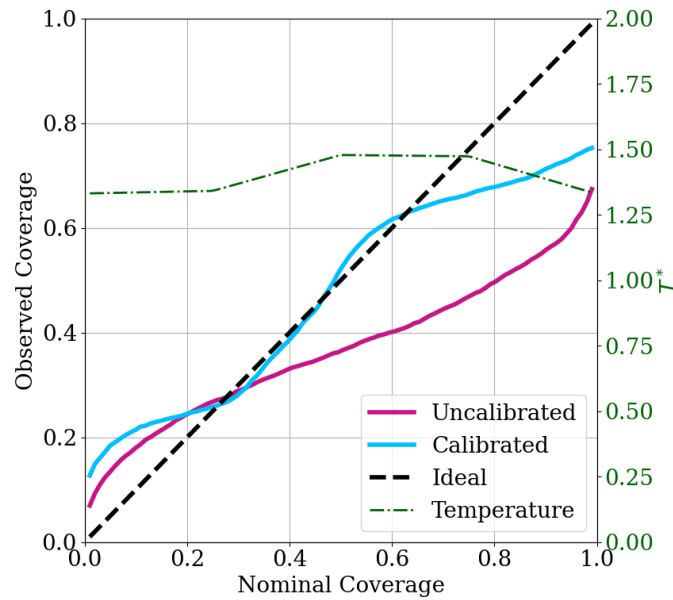


Figure 9. Comparison of the PP plots from the uncalibrated (purple) and calibrated (blue) GP predictions. The 45° black dashed line represents the ideal coverage. The green dotted-dashed line, corresponding to the secondary y-axis, shows the optimal temperature as a function of nominal coverage. The calibration temperature is fit according to Equation A1.

REFERENCES

- Bogachev, V. I., Kolesnikov, A. V., & Medvedev, K. V. 2005, *Sbornik: Mathematics*, 196, 309, doi: [10.1070/SM2005v196n03ABEH000882](https://doi.org/10.1070/SM2005v196n03ABEH000882)
- Che, Z., Purushotham, S., Cho, K., Sontag, D., & Liu, Y. 2018, *Scientific reports*, 8, 6085
- Cherubini, T., & Businger, S. 2013, *Journal of Applied Meteorology and Climatology*, 52, 498, doi: [10.1175/JAMC-D-11-0263.1](https://doi.org/10.1175/JAMC-D-11-0263.1)
- Cherubini, T., Lyman, R., & Businger, S. 2021a, *Monthly Notices of the Royal Astronomical Society*, 509, 232, doi: [10.1093/mnras/stab2916](https://doi.org/10.1093/mnras/stab2916)
- . 2021b, *Monthly Notices of the Royal Astronomical Society*, 509, 232, doi: [10.1093/mnras/stab2916](https://doi.org/10.1093/mnras/stab2916)
- Cho, K., van Merriënboer, B., Gulcehre, C., et al. 2014, *Learning Phrase Representations using RNN Encoder-Decoder for Statistical Machine Translation*. <https://arxiv.org/abs/1406.1078>
- Doersch, C. 2016, arXiv preprint arXiv:1606.05908
- Dong, G., & Liu, H. 2018, *Feature engineering for machine learning and data analytics* (CRC press)
- Frehlich, R., Sharman, R., Vandenberghe, F., et al. 2010, *Journal of Applied Meteorology and Climatology*, 49, 1742, doi: [10.1175/2010JAMC2350.1](https://doi.org/10.1175/2010JAMC2350.1)
- Giordano, C., Rafalimanana, A., Ziad, A., et al. 2020, in *Adaptive Optics Systems VII*, ed. L. Schreiber, D. Schmidt, & E. Vernet, Vol. 11448, International Society for Optics and Photonics (SPIE), 114484E, doi: [10.1117/12.2562316](https://doi.org/10.1117/12.2562316)
- Giordano, C., Rafalimanana, A., Ziad, A., et al. 2021, *Monthly Notices of the Royal Astronomical Society*, 504, 1927, doi: [10.1093/mnras/staa3709](https://doi.org/10.1093/mnras/staa3709)
- Giordano, C., Vernin, J., Trinquet, H., & Muñoz-Tuñón, C. 2014, *Monthly Notices of the Royal Astronomical Society*, 440, 1964, doi: [10.1093/mnras/stu356](https://doi.org/10.1093/mnras/stu356)
- Giordano, C., Vernin, J., Vázquez Ramió, H., et al. 2013, *Monthly Notices of the Royal Astronomical Society*, 430, 3102, doi: [10.1093/mnras/stt117](https://doi.org/10.1093/mnras/stt117)
- Goodfellow, I., Bengio, Y., & Courville, A. 2016, *Deep Learning* (MIT Press)
- Guo, C., Pleiss, G., Sun, Y., & Weinberger, K. Q. 2017, arXiv e-prints, arXiv:1706.04599, doi: [10.48550/arXiv.1706.04599](https://doi.org/10.48550/arXiv.1706.04599)
- Hochreiter, S. 1998, *International Journal of Uncertainty, Fuzziness and Knowledge-Based Systems*, 6, 107
- Hochreiter, S., & Schmidhuber, J. 1997a, *Neural Comput.*, 9, 1735–1780, doi: [10.1162/neco.1997.9.8.1735](https://doi.org/10.1162/neco.1997.9.8.1735)
- . 1997b, *Neural computation*, 9, 1735
- Jain, L. C., & Medsker, L. R. 1999, *Recurrent Neural Networks: Design and Applications*, 1st edn. (USA: CRC Press, Inc.)

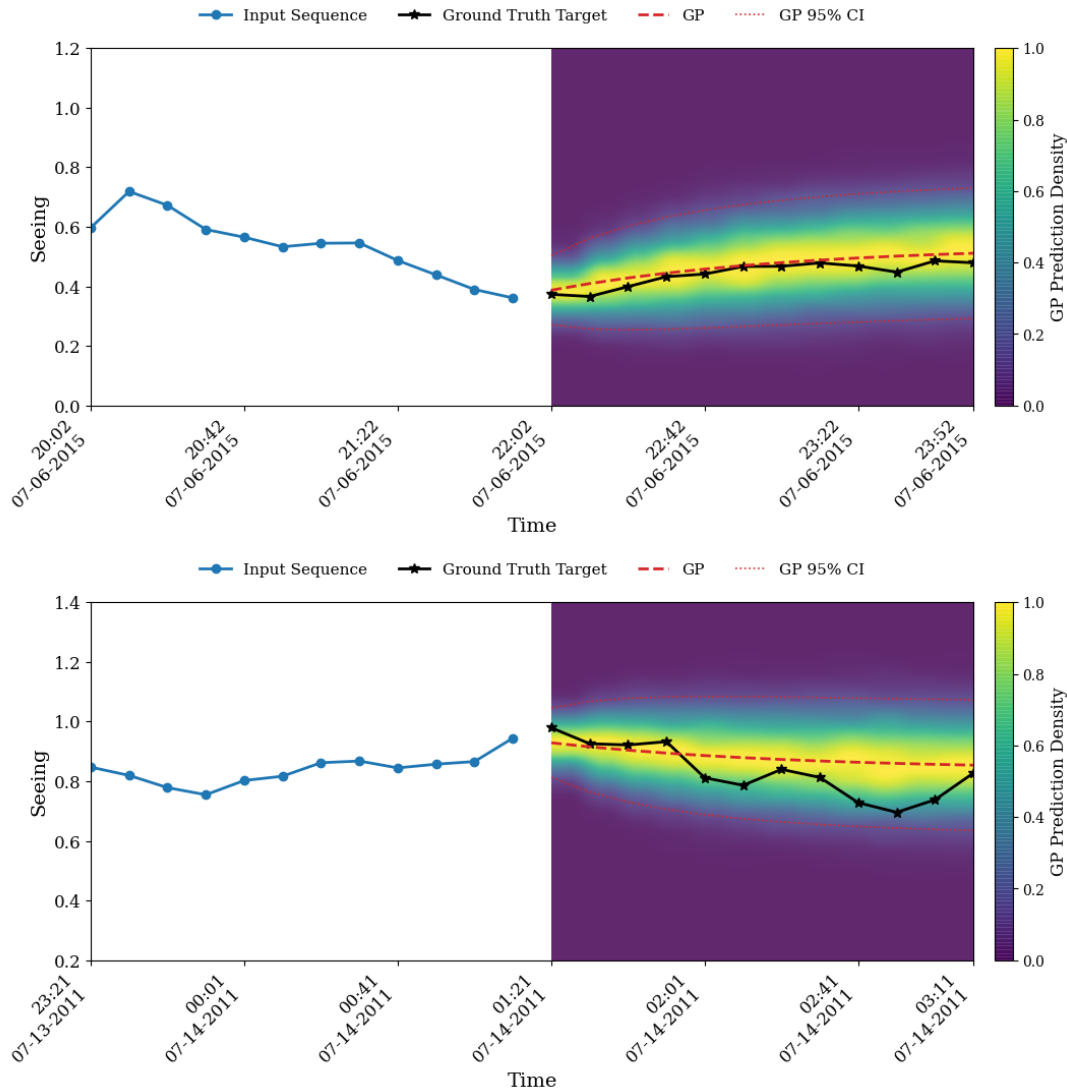


Figure 10. GP posterior predictive plots for the case studies of (a) 06 July 2015 and (b) 13 July 2011. The posterior mean is shown as a red dashed line, while the 95% confidence interval is indicated by small red dots. The input sequence is shown in blue, and the ground-truth target values are shown in black. The heatmap represents the probability density inferred from the GP posterior samples.

Jones, J., Watson, G., & Foster, G. 2004, *AIAA journal*, 42, 2438

Khalighi, M. A., & Uysal, M. 2014a, *IEEE Communications Surveys & Tutorials*, 16, 2231, doi: [10.1109/COMST.2014.2329501](https://doi.org/10.1109/COMST.2014.2329501)

—. 2014b, *IEEE Communications Surveys & Tutorials*, 16, 2231, doi: [10.1109/COMST.2014.2329501](https://doi.org/10.1109/COMST.2014.2329501)

Kornilov, M. V. 2015, *Experimental Astronomy*, 41, 223–242, doi: [10.1007/s10686-015-9485-7](https://doi.org/10.1007/s10686-015-9485-7)

Kornilov, V., Tokovinin, A., Shatsky, N., et al. 2007, *Monthly Notices of the Royal Astronomical Society*, 382, 1268, doi: [10.1111/j.1365-2966.2007.12467.x](https://doi.org/10.1111/j.1365-2966.2007.12467.x)

Lipton, Z. C., Kale, D. C., Elkan, C., & Wetzell, R. 2015, arXiv preprint arXiv:1511.03677

Lyman, R., Cherubini, T., & Businger, S. 2020, *Monthly Notices of the Royal Astronomical Society*, 496, 4734, doi: [10.1093/mnras/staa1787](https://doi.org/10.1093/mnras/staa1787)

Majumdar, A. K. 2015, *Fundamentals of Free-Space Optical (FSO) Communication System* (New York, NY: Springer New York), 1–20, doi: [10.1007/978-1-4939-0918-6_1](https://doi.org/10.1007/978-1-4939-0918-6_1)

Masciadri, E., Lascaux, F., Turchi, A., & Fini, L. 2017, *Monthly Notices of the Royal Astronomical Society*, 466, 520

Masciadri, E., Martelloni, G., & Turchi, A. 2019, *Monthly Notices of the Royal Astronomical Society*, 492, 140, doi: [10.1093/mnras/stz3342](https://doi.org/10.1093/mnras/stz3342)

- Masciadri, E., Turchi, A., & Fini, L. 2023, *Monthly Notices of the Royal Astronomical Society*, 523, 3487, doi: [10.1093/mnras/stad1552](https://doi.org/10.1093/mnras/stad1552)
- Medvedev, K. 2008, *Theory of Stochastic Processes*, 1
- Milli, J., Gonzalez, R., Fluxa, P. R., et al. 2019, *Nowcasting the turbulence at the Paranal Observatory*. <https://arxiv.org/abs/1910.13767>
- Ni, W.-J., Shen, Q.-L., Zeng, Q.-T., et al. 2022, *Research in Astronomy and Astrophysics*, 22, 125003
- Papamakarios, G., Nalisnick, E., Rezende, D. J., Mohamed, S., & Lakshminarayanan, B. 2021, *Journal of Machine Learning Research*, 22, 1
- Papamakarios, G., Pavlaku, T., & Murray, I. 2017, *Advances in neural information processing systems*, 30
- Pascanu, R., Gulcehre, C., Cho, K., & Bengio, Y. 2014, *How to Construct Deep Recurrent Neural Networks*. <https://arxiv.org/abs/1312.6026>
- Rafalimanana, A., Giordano, C., Ziad, A., & Aristidi, E. 2019, in *SF2A-2019: Proceedings of the Annual meeting of the French Society of Astronomy and Astrophysics*, Di
- Rafalimanana, A., Giordano, C., Ziad, A., & Aristidi, E. 2021, in *International Conference on Space Optics — ICSO 2020*, ed. B. Cugny, Z. Sodnik, & N. Karafolas, Vol. 11852, *International Society for Optics and Photonics (SPIE)*, 118524G, doi: [10.1117/12.2599659](https://doi.org/10.1117/12.2599659)
- Rafalimanana, A., Giordano, C., Ziad, A., & Aristidi, E. 2022, *Publications of the Astronomical Society of the Pacific*, 134, 055002, doi: [10.1088/1538-3873/ac6536](https://doi.org/10.1088/1538-3873/ac6536)
- Rasmussen, C. E. 2003, in *Summer school on machine learning (Springer)*, 63–71
- Roddier, F. 1981, in *Progress in optics*, Vol. 19 (Elsevier), 281–376
- . 1999, *Adaptive Optics in Astronomy* (Cambridge University Press). <https://books.google.fr/books?id=4n5tBN21LRsC>
- Seeger, M. 2004, *International journal of neural systems*, 14, 69
- Sherstinsky, A. 2020, *Physica D: Nonlinear Phenomena*, 404, 132306, doi: <https://doi.org/10.1016/j.physd.2019.132306>
- Silva, S. C. D. 2012, Ph.d. thesis, UNIVERSITY OF HAWAII
- Srinivasan, R., Barausse, E., Korsakova, N., & Trotta, R. 2025, *arXiv e-prints*, arXiv:2506.22543. <https://arxiv.org/abs/2506.22543>
- Tokovinin, A. 2002, *Publications of the Astronomical Society of the Pacific*, 114, 1156, doi: [10.1086/342683](https://doi.org/10.1086/342683)
- Turchi, A., Masciadri, E., & Fini, L. 2022, in *Adaptive Optics Systems VIII*, ed. D. Schmidt, L. Schreiber, & E. Vernet (SPIE), 224, doi: [10.1117/12.2629501](https://doi.org/10.1117/12.2629501)
- Tyson, R. K. 2002, *Journal of the Optical Society of America A*, 19, 753, doi: [10.1364/JOSAA.19.000753](https://doi.org/10.1364/JOSAA.19.000753)
- Vernin, J., & Munoz-Tunon, C. 1995, *Publications of the Astronomical Society of the Pacific*, 107, 265
- Villani, C. 2003, *Topics in optimal transportation, Graduate studies in mathematics* (Providence, Rhode Island: American mathematical society)
- Wang, Y., Xu, H., Li, D., et al. 2018, *Scientific Reports*, 8, 1124, doi: [10.1038/s41598-018-19559-9](https://doi.org/10.1038/s41598-018-19559-9)
- Wolf, T., Debut, L., Sanh, V., et al. 2020, in *Proceedings of the 2020 conference on empirical methods in natural language processing: system demonstrations*, 38–45
- Yu, Y., Si, X., Hu, C., & Zhang, J. 2019, *Neural Computation*, 31, 1235, doi: [10.1162/neco_a.01199](https://doi.org/10.1162/neco_a.01199)